Diamond & Related Materials 127 (2022) 109156

Contents lists available at ScienceDirect

Diamond & Related Materials

journal homepage: www.elsevier.com/locate/diamond

Ni_3S_2 nanowires filled carbon nanotubes of ultra-high quality: Synthesis methods, structure, and electrical properties

Yuba Raj Poudel [a], Xu Zhao [a,c], Katherine L. Jungjohann [b], Arun Thapa [a], Rui Guo [a], Wenzhi Li [a,*]

[a] Department of Physics, Florida International University, 11200 SW 8th Street, Miami, FL 33199, USA
[b] Center for Integrated Nanotechnologies, Sandia National Laboratories, Box 5800, Albuquerque, NM 87185, USA
[c] College of Physics, Key Laboratory of Advanced Films of Hebei Province, Hebei Normal University, 20 S 2nd Ring Rd E, Yuhua District, Shijiazhuang, Hebei 050024, PR China

ARTICLE INFO

Keywords:
Carbon nanotubes (CNTs)
Filled CNTs
Nickel sulfide (Ni_3S_2)
Ni_3S_2 nanowires
In situ filling

ABSTRACT

The synergy between the host carbon nanotube (CNT) and the guest filler distinguishes the filled CNTs as hybrid nanomaterials with unique properties. Many materials have been filled inside the CNT cores using several strategies; however, a reliable filling method to encapsulate transition metal sulfide nanowires inside the CNTs is still lacking. An *in situ* method is developed for the first time to synthesize the Ni_3S_2 nanowires filled CNTs (Ni_3S_2@CNTs), and their fundamental properties are investigated. Electron microscopy results demonstrate a core-shell structure of Ni_3S_2@CNT, *i.e.*, a CNT filled with a continuous and single-crystalline, rhombohedral Ni_3S_2 nanowire up to several micrometers in length. An exceptionally low value of the ratio between the intensities of D and G bands ($I_D/I_G = 0.26$) in the Raman spectroscopy measurements suggests that Ni_3S_2@CNTs are very well graphitized, possessing an ultra-high quality. A mean resistivity of 6.1×10^{-5} Ωm is estimated using both two probe and four-point probe measurements on individual Ni_3S_2@CNTs. Also, a diameter selective electrical breakdown or emptying of the filled nanotube channel is observed as higher currents pass through an individual Ni_3S_2@CNT.

1. Introduction

Carbon nanotubes (CNTs) are formed due to the rolling up of one or many graphitic layers in a concentric manner [1]. When a graphene layer converts into a one-dimensional cylindrical structure having a nano-scaled diameter, it brings about novel physical properties in CNTs. For example, a particular CNT can have metallic or semiconducting properties depending on its diameter and helicity [2,3], which are different from the electronic properties of semi-metallic graphene/graphite [4,5]. To date, CNTs have garnered a high level of attention given their unique electronic [2], mechanical [6], and thermal [7] properties attractive for various applications.

In addition to the fundamental physical properties owned by CNTs, many strategies have been put forward to enhance them further and broaden their real-life applications. Among many, the filling of the CNT interior remains an attractive method since it can synergize the qualities of both the CNT and the filling material [1]. Thanks to the unique tubular structure of CNT that offers the possibility of filling its hollow core with a variety of inorganic and organic materials to form different nanohybrids. These nanohybrids can be visualized as nanocapsules or nanococcons containing carbon shell(s) encasing another material in different forms such as nanoparticles (NPs), nanorods, nanowires, *etc.* The encapsulation of foreign materials in the empty cores of CNTs allows a blending of the properties of host CNTs and guest fillers bringing unusual electrical [8,9], magnetic [10,11], electromagnetic [12–14], electrochemical [15,16], and optical properties [17,18] among the filled CNTs (X@CNTs [19], where X is an arbitrary filler). Filled CNTs with such unique behavior have shown promising applications in energy storage devices, electromagnetic shielding, sensors, filters, memory devices, nano biomedical devices, *etc.* [1].

There are two different methods of filling CNTs which are widely known as *ex situ* filling and *in situ* filling [1,19]. *Ex situ* filling or post-synthesis filling is a multi-step filling process whereas an *in situ* filling is a single-step filling process in which CNTs are synthesized and filled simultaneously. The *in situ* filling is a sophisticated method that enables a complete filling of the CNT core whereas the *ex situ* method usually generates a partial and discontinuous filling. Unlike *ex situ* filling, the *in situ* filling method does not require any chemical or thermal treatment to

* Corresponding author.
E-mail address: wenzhi.li@fiu.edu (W. Li).

https://doi.org/10.1016/j.diamond.2022.109156
Received 15 April 2022; Received in revised form 28 May 2022; Accepted 2 June 2022
Available online 6 June 2022

open the CNT tips which can compromise the quality of filled CNTs. Moreover, it's a more reliable and efficient method due to the ease of control over the filling parameters involved in the one-step process.

Until today, numerous inorganic [12,13,15,20–23] and organic materials [24–26] have been encapsulated inside CNT cores, however, most of them were attained through *ex situ* methods. There still exists a serious challenge in the detailed study of the filled CNTs due to a very low quantity of filled CNTs that can be synthesized using the existing *ex situ* techniques. Another difficulty persists in the substrate nature itself which usually limits the applications of the filled CNTs. Last but not the least barrier remains the quality of the filled CNTs which plays a vital role in their physical properties such as mechanical strength, thermal resistance, electrical conductivity, chemical reactivity, *etc.* Thus, there exists a dire need for an upscaled and reliable *in situ* method that can be implemented to synthesize filled CNTs of high quality in different substrates capable of practical applications.

Nanostructured nickel sulfides possess interesting and useful physical properties and have remained on research focus for the past few decades, however, they haven't been filled inside CNTs previously and thus the fundamental properties of nickel sulfide filled CNTs are still unclear. There are many stable phases of nickel sulfide including simplest to more complex forms such as α-NiS, β-NiS, NiS_2, Ni_3S_2, Ni_3S_4, Ni_7S_6, Ni_9S_8, $Ni_{17}S_{18}$, *etc.* [27,28]. Amidst different members of the nickel sulfide family, Ni_3S_2 (heazlewoodite) has attracted many researchers and scientists due to its intrinsic metallic behavior, high abundance, high stability, high energy storage capacity, environmentally benign behavior, and exceptional catalytic properties [29–31]. It has been established that the physical properties of Ni_3S_2 can be boosted by integrating it with carbonaceous materials. For example, Guan et al. [30] found that Ni_3S_2 nanocrystals covered with a few layers of carbon and anchored on graphene sheets can provide discharge capacities up to 850 $mAhg^{-1}$ and 630 $mAhg^{-1}$ at current densities of 200 and 5000 mAg^{-1}, respectively during anode application for LIBs. The performance enhancement of Ni_3S_2 is due to the wrapping effect by C layers which can avoid the damage and degradation of Ni_3S_2 nanocrystals during charge-discharge processes. Similarly, another study [29] shows that carbon-coated Ni_3S_2 nanowires act as efficient and highly stable electrocatalysts for hydrogen evolution reactions exhibiting a potential of about 199 mV at 10 $mAcm^{-2}$ at a current density of 20 $mAcm^{-2}$.

There are two main advantages of filling Ni_3S_2 nanowires inside CNTs. First, Ni_3S_2 itself possesses intrinsic metallic behavior with a measured resistivity of 1.2×10^{-6} Ωm [32], which can dramatically change the electrical properties of CNTs facilitating the charge transportation along the Ni_3S_2@CNTs. The other advantage is that the robust walls of CNTs can inhibit or prevent the Ni_3S_2 filler from any damage or degradation during several applications. Thus, it is expected that Ni_3S_2@CNTs exhibit unique physical properties and can find numerous applications in next-generation electronic devices and electrochemical systems.

Here, we describe a novel *in situ* method to synthesize multi-walled CNTs filled with nickel sulfide nanowires (Ni_3S_2@CNTs) directly on both porous and non-porous substrates using two different catalyst precursors. The first approach can be used to synthesize Ni_3S_2@CNTs on Si substrates with control over their lengths and diameters whereas the second approach can be used to synthesize a significant mass of Ni_3S_2@CNTs on conductive nickel foam (NiF) and carbon cloth (CC) substrates. Both techniques lead to the growth of high-quality CNTs completely and continuously filled with Ni_3S_2 nanowires up to several micrometers in length. Besides the material synthesis procedure, we also present a detailed characterization of Ni_3S_2@CNTs using several techniques and communicate their intrinsic electrical properties.

2. Materials and methods

2.1. Materials

Nickel nitrate hexahydrate (Ni $(NO_3)_2{\cdot}6H_2O$, 99 % pure) was purchased from Fisher Scientific International, Inc. and Ni NPs (99.9 %, 40 nm, metal basis) were purchased from US Research Nanomaterials, Inc. Ni foam (99.99 %, 1.6 mm thick, 80–100 pores per inch) was purchased from MTI Corporation and carbon cloth (CeTech carbon cloth without microporous layer) having a thickness of 330 μm was purchased from the Fuel Cell Store. All reagents including isopropyl alcohol (IPA), acetone, and ethanol were purchased from Fisher Scientific and were used as received. Thiophene (C_4H_4S) – the precursor for carbon and sulfur, of extra pure grade (99+ %) was purchased from Acros Organics. Empty multi-walled CNTs (used as a reference in this work) were synthesized using a method similar to that reported in the literature [33,34]. Briefly, CNTs were synthesized on iron/silica substrates by the pyrolysis of acetylene. The iron/silica substrates were formed by a sol-gel process in which tetraethoxysilane and iron nitrate aqueous solution were used as the precursors and concentrated hydrogen fluoride was used as an additive to control the gelation speed. After gelation, the gel was dried overnight at about 100 °C to form substrates, then the substrates were calcined at 450 °C overnight. For the carbon nanotube synthesis, the substrates were reduced at 550 °C for 5 h in a flow of 9 % H_2/N_2 with a flow rate of 110 cm^3/min to yield iron nanoparticles on the surface of silica. Subsequently, carbon nanotubes were produced on the substrates in a flow of 9 % acetylene in nitrogen with a 110 cm^3/min flow rate at 650 °C for 24 h. Au electrodes (both two and four probes) were pre-patterned on a SiO_2/Si wafer using photolithography to conduct the electrical measurements. To construct a nanodevice for *in situ* electrical measurements, Ni_3S_2@CNTs were scraped from the substrate using a razor blade and affixed to an Al wire using conductive epoxy.

2.2. Synthesis of Ni_3S_2@CNTs via nickel salt

Ni $(NO_3)_2{\cdot}6H_2O$ was crushed and mixed with IPA to make three different catalyst solutions of concentrations 0.02 M, 0.04 M, and 0.06 M. Silicon substrates were cleaned and coated with the catalyst solution using a two-stage spin coating (850 rpm for 60 s and 2000 rpm for another 60 s) to achieve a uniform thin layer of catalyst particles.

Firstly, catalyst solution-coated Si substrates were heated in the air in a furnace at 600 °C for 30 mins to oxidize the catalyst layer. Afterward, Ar and H_2 were passed through the chamber, both at a flow rate of 100–200 sccm for 15 mins, to reduce the catalyst oxide to metallic catalyst. After reduction, H_2 flow was stopped and Ar was continued to flow in the chamber until the desired synthesis temperature (1000 °C–1200 °C) was reached. Then, Ar was flown at an increased concentration (1650–1850 sccm) and H_2 flow (100–200 sccm) was also resumed. However, H_2 was flown through a new path such that it could bubble through the thiophene, carrying the carbon and sulfur precursor to the reaction chamber. The synthesis was carried out for 10–30 min where the graphitization of carbon walls and filling of the interior with Ni_3S_2 nanowires could coincide simultaneously. The chamber was naturally cooled down in an inert atmosphere after the synthesis was completed.

2.3. Synthesis of Ni_3S_2@CNTs via nickel nanoparticles

Since the growth scale of Ni_3S_2@CNTs was limited on Si substrates, another method was developed to synthesize a large number of Ni_3S_2@CNTs on three-dimensional NiF) and carbon cloth (CC) substrates. To begin with, a dispersion of desired concentration (2–100 gl^{-1}) was created using Ni nanoparticles and IPA. It was then placed in an ultrasonication bath for 5 min to make the suspension uniform and was transferred to a clean vial. NiF or CC substrates were cut into small

pieces *e.g.*, roughly 2 cm × 2 cm in size (note: any size and shape of the substrate can be chosen which fits in the system) and were cleaned in an ultrasonication bath. The NiF or CC substrates were immersed in the IPA- Ni NPs suspension for 5 min. The vial was gently stirred to prevent the agglomeration of Ni NPs during the dip-coating process. Afterward, the substrates were heated at 150 °C for 5 min using a hot plate to evaporate the IPA. The CVD growth of Ni_3S_2@CNTs was carried out on the NiF or CC substrates as described in Section 2.2, however, a pre-treatment was required for NiF substrates. The pretreatment process was a complete synthesis process with similar experimental conditions but in the absence of Ni catalyst particles. The role of the pre-treatment on NiF substrates is discussed in Section 3.2. It is very important to note that CC substrates do not require any pre-treatment process such as heat treatment, chemical activation, plasma treatment, *etc.* They can be used in pristine form to load the catalyst particles and subsequently synthesize Ni_3S_2@CNTs in one step. During the synthesis *via* Ni NPs, the first step (oxidation in the air) was eliminated in both substrates since the catalysts were pure metal NPs.

2.4. Characterization techniques

Field Emission Scanning Electron Microscope (FESEM) JEOL JSM-6330F and JSM-F100 Schottky FESEM were used to obtain the SEM images on an accelerating voltage of 15–25 kV. Transmission electron microscopy (TEM) images, energy dispersive X-ray (EDX) spectra, and selected area electron diffraction (SAED) patterns were acquired by using FEI Tecnai F30 TEM, Tecnai G^2 20 U-Twin high-resolution TEM, and FEI Talos F200X TEM equipped with EDAX, operating at an accelerating voltage of 200 kV. Siemens Diffraktometer D5000 with Cu Kα radiation (λ = 1.54 Å) was used to acquire the XRD profiles of powder samples. Raman measurements were made using a laser wavelength of 632.8 nm in a Raman microscope setup as described in the reference [35]. Agilent Technologies Cary Series UV–Vis-NIR spectrophotometer was used to collect the UV–Vis spectra. Fourier Transform Infrared Spectroscopy (FTIR) was performed using JASCO FTIR-4100 whereas the Thermogravimetric Analysis (TGA) was carried out in SDT Q600. The tips of Ni_3S_2@CNTs were opened using Harrick plasma cleaner. The electrical characterizations were performed using Keithley 2400 Source meter and the *in situ* electrical tests were performed inside a Thermo Fisher Scientific Titan G2 ETEM at 300 kV with a Gatan K3-IS high-speed direct electron camera.

3. Results and discussions

3.1. Ni_3S_2@CNTs synthesized via nickel salt

Fig. 1 (a-c) show the SEM images of a small section of the catalyst layer (0.06 M concentration) on Si substrate after dispersion, oxidation, and reduction, respectively, and a typical particle in each case is shown in Fig. 1(d-f), respectively. The smooth surface (dome-shaped structure) as observed in Fig. 1d undergoes a surface fracture forming a rose-like multi-layered structure after air oxidation at 600 °C which is shown in Fig. 1e. Fig. 1f shows the further evolution of the particle surface (formation of clusters) after reduction by H_2 gas. Figs. 1 (g-i) are the high magnification SEM images showing the details of the particle surface after dispersion, oxidation, and reduction, respectively. The evolution of the catalyst can be understood as the following. Firstly, the as-dispersed nickel nitrate hexahydrate particle (shown in Fig. 1g) decomposes after heat treatment and converts into nickel oxide (NiO) at around 573 °C. Meanwhile, the high temperature also causes surface modification (fissures on the particle surface) as shown in Fig. 1h. During the reduction by H_2 gas, NiO converts into metallic Ni along with a further surface modification as shown in Fig. 1i. In the synthesis process, the furnace temperature rises further causing the further dissociation of big Ni clusters (shown in Fig. 1i) into smaller Ni NPs which act as the final catalysts for the growth of Ni_3S_2@CNTs.

Fig. 2 shows the SEM images of Ni_3S_2@CNTs synthesized on Si substrates using different concentrations of catalyst solution. Figs. 2 (a-c) show the low magnification SEM images and Figs. 2 (d-f) show the high magnification SEM images of samples obtained using catalyst precursors of concentrations 0.02 M, 0.04 M, and 0.06 M, respectively. All growth conditions were identical where the flow rates of H_2 and Ar

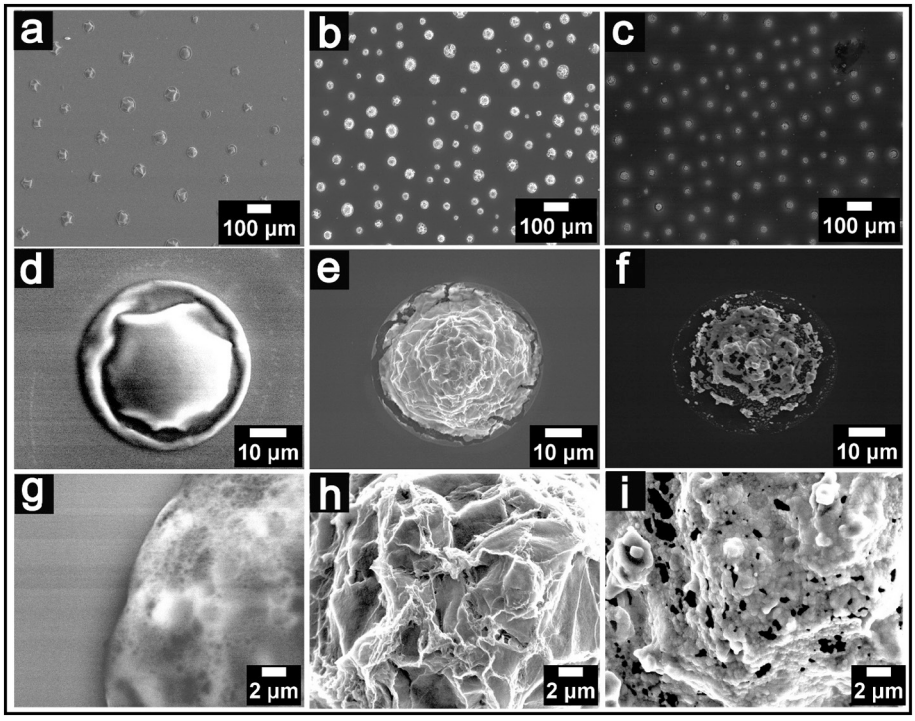

Fig. 1. SEM images (low magnification) of 0.06 M catalyst particles after (a) dispersion (b) oxidation (c) reduction; (d-f) a representative particle after dispersion, oxidation and reduction, respectively; (g-i) SEM images (high magnification) of a representative particle after dispersion, oxidation and reduction, respectively.

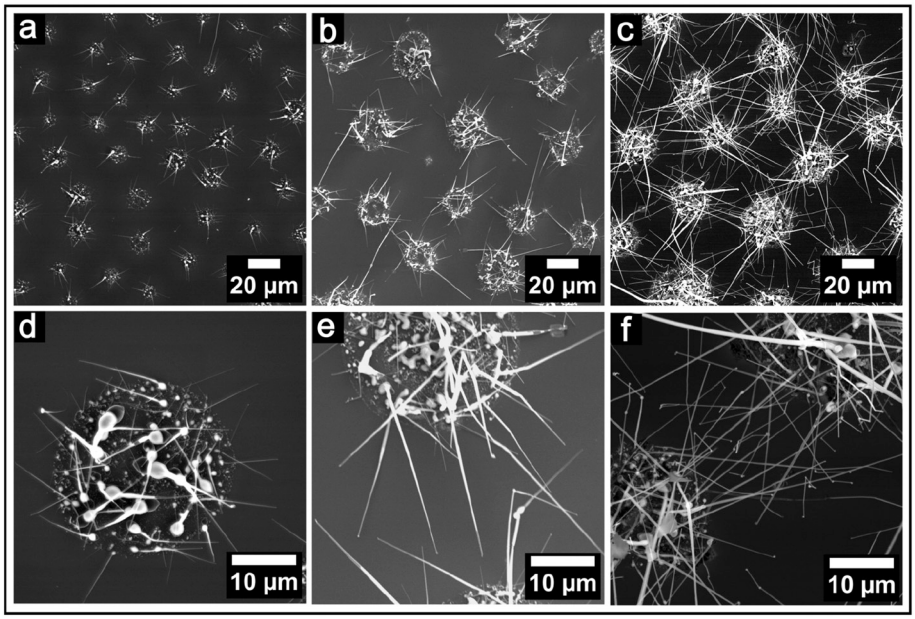

Fig. 2. SEM images of Ni_3S_2@CNTs synthesized using $Ni(NO_3)_2{\cdot}6H_2O$ - IPA of concentrations 0.02 M (Figure a and d), 0.04 M (Figure b and e), and 0.06 M (Figure c and f), respectively.

were 115 sccm and 1700 sccm, respectively, and the synthesis was carried out for 15 min at 1000 °C.

It is clear from Fig. 2 (d-f) that Ni_3S_2@CNTs have a linear and tapering structure which is very unique compared to empty MWCNTs which are typically curved and intertwined due to hollow cores which causes radial buckling. To understand the effect of the concentration of the catalyst precursor, lengths and diameters measurements were performed on100 different Ni_3S_2@CNTs synthesized from each concentration. As the catalyst concentration increased, Ni_3S_2@CNTs became longer and thicker without any effect on the morphology. The histogram in Fig. S1 shows the distribution of lengths and diameters of Ni_3S_2@CNTs synthesized using three different concentrations of the catalyst precursor. Also, it was established that the optimized catalyst concentrations for the growth of Ni_3S_2@CNTs on Si substrates lie in the 0.02 M- 0.06 M range (See Fig. S2 for the results obtained from lower and higher concentrations). However, higher concentrations of the catalyst can be used to synthesize Ni_3S_2@CNTs on other substrates such as carbon cloth as shown in Fig. S3.

3.2. *Ni_3S_2@CNTs synthesized via nickel nanoparticles*

The synthesis of Ni_3S_2@CNTs *via* nickel salt offers control over the dimensions of Ni_3S_2@CNTs, however, this method suffers two serious challenges. First, it cannot be upscaled to synthesize a significant quantity of Ni_3S_2@CNTs and the other drawback arises from the poor electrical conductivity of the substrate itself. To solve these problems,

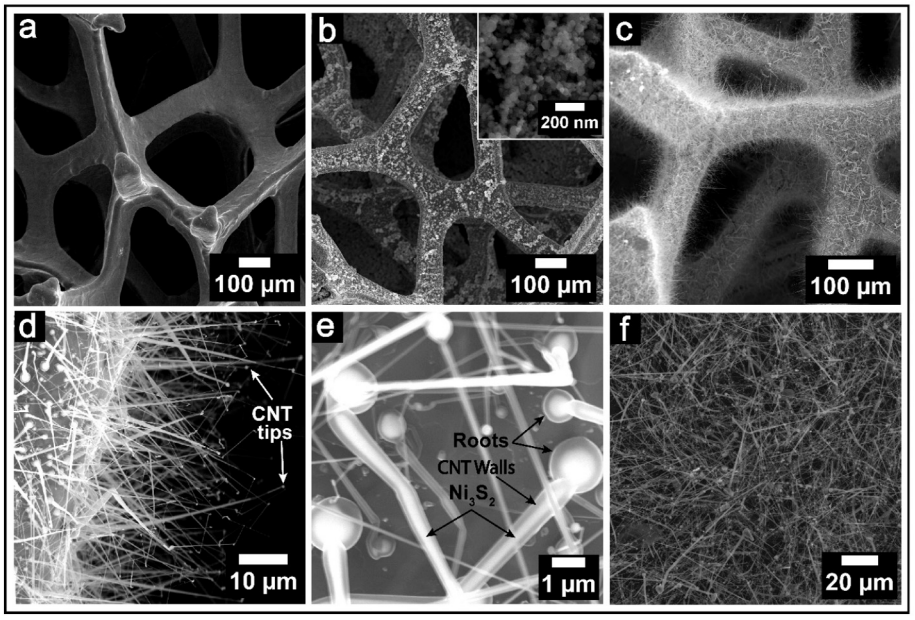

Fig. 3. Low magnification SEM image of (a) pristine NiF, (b) NiF after dip-coating (inset shows deposition of Ni NPs), and (c) NiF after the growth of Ni_3S_2@CNTs. (d) SEM image showing the linear structure of Ni_3S_2@CNTs. (e) High magnification SEM image showing CNTs and the filler Ni_3S_2 (f) SEM image of Ni_3S_2@CNTs after extraction from the NiF substrates.

we have advanced the synthesis of Ni_3S_2@CNTs in other useful substrates such as NiF and CC using Ni NPs as the catalyst precursor. It is desired to synthesize Ni_3S_2@CNTs on NiF as it has unique features such as high specific surface area along with a multilayered porous structure, high intrinsic strength, lightweight, good electrical and thermal conductivity, *etc.* Fig. 3 shows the SEM images of Ni_3S_2@CNTs synthesized on NiF (Ni_3S_2@CNTs/ NiF). As mentioned before, the growth of Ni_3S_2@CNTs was not observed in pristine NiF dip-coated with Ni catalyst particles and a pre-treatment to the substrate under the same growth conditions in the absence of Ni catalyst NPs was necessary for the synthesis of Ni_3S_2@CNTs. The main reason behind this situation can be that Ni NPs liquefy and sink at the surface of the NiF resulting in the loss of the catalytically active Ni NPs at high temperatures. However, if the NiF is pretreated, a layer of Ni_3S_2 and carbon can form on its surface which acts as the barrier between the NiF surface and Ni NPs and prevent the dissolution of the Ni NPs into the NiF. The formation of Ni_3S_2 and carbon on the NiF surface after a pretreatment under identical experimental conditions was confirmed by comparing the XRD spectra of pristine NiF and pre-treated (sulfidized) NiF as shown in Fig. S4. Fig. 3a shows a section of a pristine NiF and Fig. 3b shows a similar section after dip-coating the NiF substrate in Ni NPs-IPA suspension. Given the porous and three-dimensional structure of NiF, it can be loaded with a larger quantity of Ni NPs, however, the catalyst loading can be controlled by one's choice by changing the concentration of the Ni NPs-IPA suspension. For example, 10.19 mg of Ni NPs can be loaded on a particular NiF substrate 2 cm × 2 cm, as shown in Fig. 3b, after dip-coating with a suspension having a concentration of 80 gl^{-1}.

The SEM images in Fig. 3 (c-e) show that almost all Ni catalyst particles take part in the growth of the nanotubes. Fig. 3f shows a thin film of Ni_3S_2@CNTs deposited on a Si substrate after the samples were extracted from NiF substrates using an ultrasonication process.

It is also desirable to synthesize Ni_3S_2@CNTs on another useful substrate that can offer other unique features and eliminate the requirement of the substrate pretreatment. Among many, carbon cloth (CC) substrate remains an attractive substrate material due to its high modulus, high flexibility, electrical conductivity, thermal stability, low weight, low density and high chemical resistance against oxidation and corrosion and can be extremely useful for electrochemical and electromagnetic applications [36,37]. Furthermore, the woven geometry of a CC substrate provides an additional geometric enhancement effect during several applications [38]. In this work, we present the first example of the synthesis of filled CNTs on CC substrates. The applications of Ni_3S_2@CNTs synthesized on NiF and CC substrates can be envisioned as electrodes for lithium-ion batteries, electrochemical water splitting systems, *etc.* On the other hand, the Ni_3S_2@CNTs extracted from the substrates can find the applications as conductive additives for electrode materials. Fig. 4a shows a section of a pristine CC substrate containing a stack of several carbon threads which can be loaded with Ni NPs catalysts by a dip-coating method. Such loading of catalyst particles can be seen in Fig. 4b where Ni NPs appear to attach to each carbon thread. This loading density, however, can be controlled by changing the concentration of Ni NPs-IPA suspension. For example, one shown in Fig. 4b was achieved using a 20 gl^{-1} concentration of the catalyst particles, however, we have observed a successful growth using any catalyst concentration in the range of 2–100 gl^{-1}. It was found that the catalyst concentration is directly related to the quantification of Ni_3S_2@CNTs, meaning that we can control the mass and growth density of Ni_3S_2@CNTs on the CC substrate by changing the concentration of Ni NPs suspension. Fig. 4c shows a high magnification SEM image of a cluster of Ni NPs with an average diameter of 40 nm dispersed on the CC substrate. It is important to understand that these smaller catalyst particles can melt and fuse together at higher temperatures to form bigger Ni NPs (several hundred nanometers to 1 μm) which are the actual catalysts for the nucleation and growth of Ni_3S_2@CNTs. Fig. 4d and e show the uniform growth of Ni_3S_2@CNTs on the CC substrate (Ni_3S_2@CNTs/ CC). Alike Ni_3S_2@CNTs/Ni-F, Ni_3S_2@CNTs/CC also possess the core-shell structure and the Ni_3S_2@CNTs can be easily collected in powder/cluster form through the ultrasonication of the Ni_3S_2@CNTs/ CC for 5–10 min as shown in Fig. 4f. It was also observed that CC substrate being inert in nature remains unchanged after pretreatment under identical experimental conditions, whereas NiF substrates would produce a change in mass due to the formation of Ni_3S_2 and C layers.

3.3. *Microstructure of Ni_3S_2@CNTs*

The TEM images of Ni_3S_2@CNTs synthesized on NiF substrates using 40 nm Ni NPs are shown in Fig. 5. Fig. 5a demonstrates the reliability of

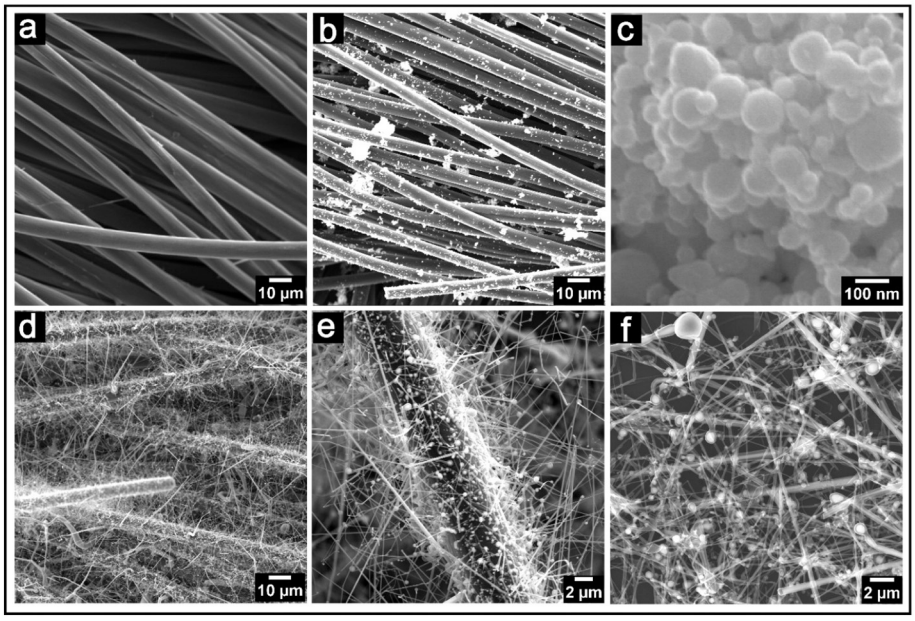

Fig. 4. SEM images of (a) pristine CC and (b) CC after loading Ni NPs catalysts. (c) High magnification SEM image of as-dispersed Ni NPs. (d-e) SEM images of Ni_3S_2@CNTs/CC at different magnifications, and (f) SEM image of Ni_3S_2@CNTs collected *via* ultrasonication and deposited on a Si wafer by spin-coating.

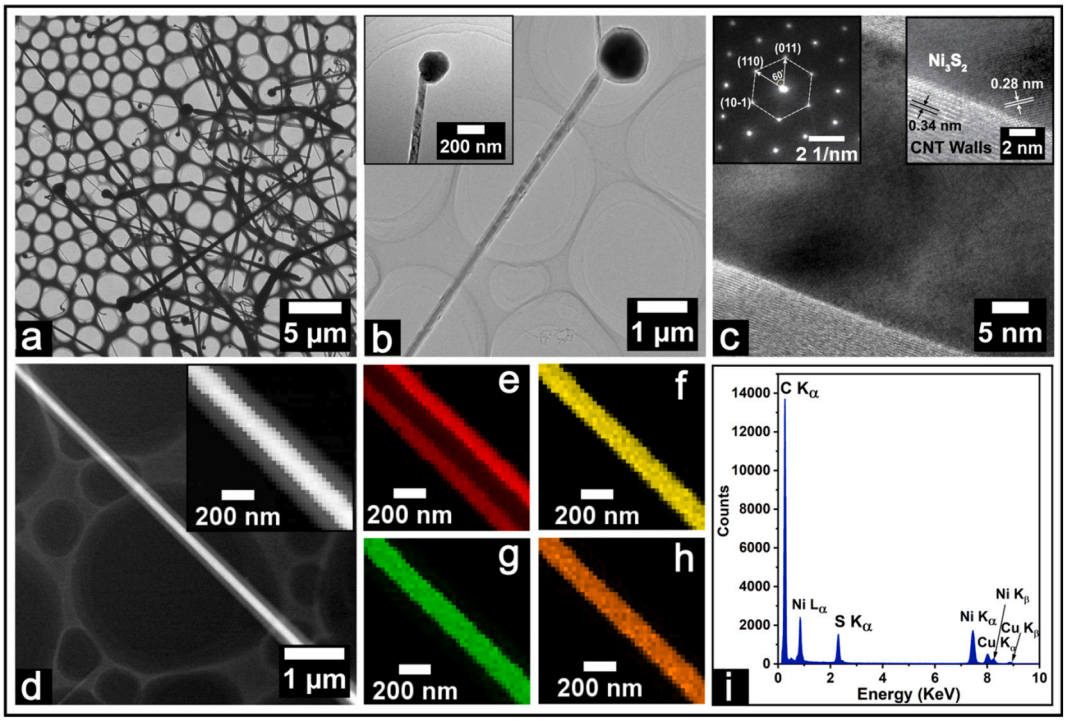

Fig. 5. (a) TEM image (low resolution) showing Ni_3S_2@CNTs. (b) TEM image (low resolution) of a typical Ni_3S_2@CNT; inset shows the particle at the tip. (c) HRTEM image of a Ni_3S_2@CNT; insets show the SAED diffraction pattern and lattice fringes. (d) Drift corrected STEM image; inset shows the high-angle annular dark-field imaging (HAADF)-STEM image. (e-h) EDX elemental mapping of C-K, Ni-K, Ni-L, and S-K, respectively, and (i) EDX spectrum.

the method showing a complete filling of almost every CNT. The fragmentation observed in some Ni_3S_2@CNTs is due to the ultrasonication process which was used to collect samples for TEM studies. The TEM image of an individual Ni_3S_2@CNT with a spherical root is shown in Fig. 5b while the inset shows the closed tip structure of Ni_3S_2@CNT.

Fig. 5c shows the high-resolution TEM image of a Ni_3S_2@CNT having a smaller diameter (nanowire diameter of 36 nm and overall nanotube diameter of about 100 nm), however, the diameters of some Ni_3S_2@CNTs can exceed 500 nm (shown in later sections). The continuum of lattice planes observed on either side of the nanotube-filler interface reveals a complete filling in the radial direction too. The inset on the right side of Fig. 5c shows the fringe separation of the outer case is 0.34 nm which matches with the (002) plane of graphitic carbon whereas the spacing of 0.28 nm of the inner core matches with the d-spacing of (110) plane of rhombohedral Ni_3S_2- heazlewoodite phase (a = 5.745 A° and c = 7.135 A°; space group R32 (155); ICDD reference card No: 00–044-1418). The single crystalline nature of the filler Ni_3S_2 can be observed in the selected area electron diffraction (SAED) pattern (inset on the left side of Fig. 5c) obtained at the nanotube core. The spots were indexed as (011), (110), and (10-1) planes of Ni_3S_2 along the [1–11] zone axis. Fig. 5d shows the drift corrected STEM image of a Ni_3S_2@CNT about 350 nm thick; the inset shows its high-angle annular dark-field imaging (HAADF) STEM image. The elemental mapping of C-K, Ni-K, Ni-L, and S-K are shown in Fig. 5 (e-h), respectively and the corresponding EDX spectra are shown in Fig. 5i. It clearly shows three peaks corresponding to Ni (K_α at 7.470 keV, K_β at 8.262 keV and L_α at 0.851 keV) and a K_α peak corresponding to S at 2.306 keV. Other peaks correspond to Cu and C which are from the TEM copper grid and the CNT walls, respectively. The above research results indicate that the synthesized materials are Ni_3S_2@CNTs. Also, Ni_3S_2@CNTs synthesized on Si using nickel salt exhibited a similar microstructure which is shown in Fig. S5.

The growth of Ni_3S_2@CNTs is catalyzed by the Ni metal catalyst and promoted by the metal sulfide filler. A recent study [39] shows that sulfur can combine with the metal catalyst to form metal sulfide in the vicinity of the metal surface and intensify the atomic carbon diffusion, which, in turn, accelerates the CNT growth. As the Ni metal converts to Ni_3S_2, a high-volume expansion can occur and extrude the filler in form of a long nanowire. The growth of the CNT walls and filling of the interior are simultaneous processes; however, the actual growth mechanism is still unclear. Further investigation is necessary to understand the growth process which can explain the simultaneous growth and filling as well as the reason why Ni_3S_2@CNTs bear a tapering structure with thick roots and sharp tips.

3.4. XRD, Raman spectroscopy, and UV–vis spectroscopy

XRD measurements were performed on the powder samples collected from the NiF and CC substrates. The diamond symbols in **Fig. 6**a represent the diffraction patterns indexed as (101), (110), (003), (021), (113), (211), (104), (122), (131), (214), and (401) planes of rhombohedral Ni_3S_2 (ICDD reference card No: 00-044-1418) which correspond to the 2θ values of 21.75°, 31.10°, 37.77°, 38.27°, 49.73°, 50.12°, 54.61°, 55.16°, 69.27°, 73.04°, and 77.89°, respectively. A strong peak observed at 26.36° corresponds to the (002) plane of graphite (CNT). The three peaks labeled as (111), (200), and (220) and marked with star symbols show the diffraction patterns of Ni corresponding to the 2θ values of 44.50°, 51.84°, and 76.36°, respectively. The presence of Ni in the XRD profile of Ni_3S_2@CNTs is due to the unreacted metallic Ni catalyst particles present at the root of each Ni_3S_2@CNT. Also, similar XRD patterns were observed for the Ni_3S_2@CNTs collected from the CC substrates as shown in Fig. S6.

The Raman spectra of empty multi-walled CNTs and Ni_3S_2@CNTs in a frequency range of 120–2750 cm^{-1} are shown in Fig. 6b. The peak positions of D, G, and G' bands located at 1348 cm^{-1}, 1597 cm^{-1}, and 2683 cm^{-1}, respectively, for both samples, agree well with the literature data [40,41]. The features from the G band of CNTs arise due to the vibrations of sp^2 bonded C atoms in a honeycomb-like lattice structure. On the other hand, the D band is related to the vibrations of sp^3 carbon-containing impurities, broken sp^2 bonds, lattice distortion, *etc.*

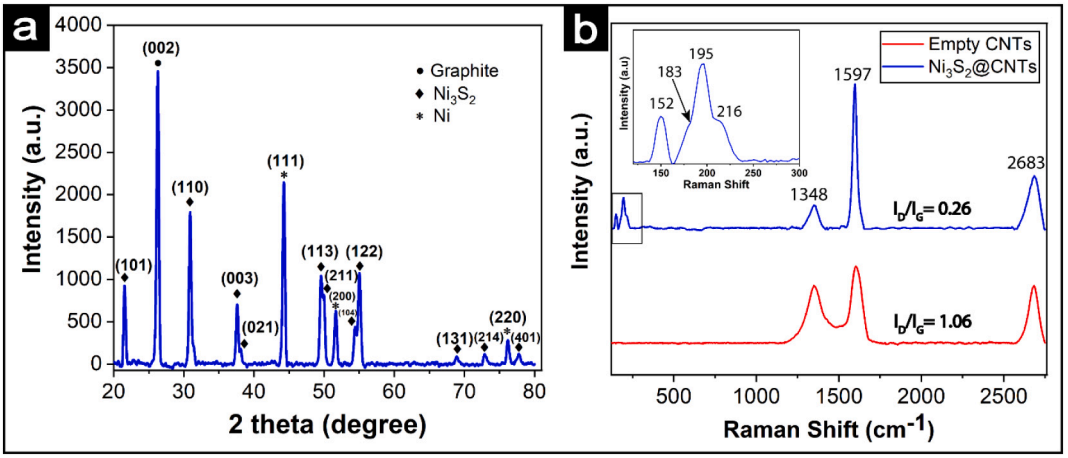

Fig. 6. (a) X-ray diffraction patternof Ni_3S_2@CNTs, (b) Raman measurements of empty* and Ni_3S_2 filled CNTs.
* Empty CNTs are independent of the filled CNTs and are only used as a reference to show the Raman characteristics of typical empty MWCNTs.

[30,41,42]. We observed a very low I_D/I_G ratio of 0.26 from Ni_3S_2@CNTs which confirms a high degree of crystallinity and quality of the CNTs. To the best of our knowledge, no report has ever reached this low I_D/I_G ratio for filled multi-walled CNTs. The key factors for such a high quality of Ni_3S_2@CNTs are the high temperature of the CVD system, continuous supply of H_2 gas during the synthesis which can eliminate the deposition of amorphous carbon, and the *in situ* nature of the filling process itself. Unlike empty CNTs, Ni_3S_2@CNTs show different Raman characteristics at lower frequencies due to the presence of Ni_3S_2 nanowire at the interior of CNTs. The Raman bands (183, 195, and 216 cm^{-1}) shown in the inset of Fig. 6b match well with the literature data [29,43,44] which are related to the Raman active phonon modes of Ni_3S_2. The other three bands of Ni_3S_2 at around 302, 320, and 348 cm^{-1} reported in the literature were absent in our measurements which can be due to their dependence on the laser excitation wavelength or any sort of nanotube-filler interaction. The band observed at 152 cm^{-1} is due to the stray light.

Fig. 7 shows the optical absorption properties of Ni_3S_2@CNTs. Samples with four different concentrations (12.5, 25, 50, and 100 mgl^{-1}) were prepared using CNTs and ethanol. The suspension was made uniform with help of an ultrasonication bath and UV–Vis measurements were performed immediately. For empty CNTs (Fig. 7a), broad absorption peaks were observed at 276 nm along with a continuous drop of absorption over wavelengths which agrees well with the literature data [45–47] for empty MWCNTs. The broad absorption feature is the result of the collective oscillation of free electron gas (π-plasmons) in the conduction band of CNTs [48,49]. On the other hand, Ni_3S_2@CNTs exhibited unique UV–Vis features arising from the synergistic effects between the CNT shells and Ni_3S_2 filler as shown in Fig. 7b. The broad peak disappeared as the π-plasmons resonance could not occur due to the transfer of charges from CNT shells to the Ni_3S_2 filler. It has recently been observed in a study [50] that there occurs a negative shift in the binding energy of the S $2P_{3/2}$ spectrum of Ni_3S_2 after wrapping it with a graphene layer. Also, electron transfer can occur from graphene to Ni_3S_2 which was revealed by the observation of C−S bond in the C 1s spectrum. Besides the unique UV–Vis spectra of Ni_3S_2@CNTs, a linear dependence of absorption on the concentration of both empty and filled CNTs (Fig. S7) was observed which is in agreement with Beer-Lambert law [45].

3.5. FTIR and TGA analysis

Fig. 8 shows the Fourier Transform Infrared Spectroscopy (FTIR) and Thermogravimetric Analysis (TGA) of the Ni_3S_2@CNTs. In the FTIR shown in Fig. 8a, a strong peak obtained at 1032 cm^{-1} can be assigned to the S═O stretching of sulfoxide [51] formed by the presence of sulfur inside the reaction chamber during the synthesis of Ni_3S_2@CNTs. The peaks at 1098 cm^{-1} and 1150 cm^{-1} can be assigned to the C-O stretching [52] whereas the peak located at 1368 cm^{-1} is due to the S═O stretching of sulfonate. Similarly, the peak at 1454 cm^{-1} is related to the

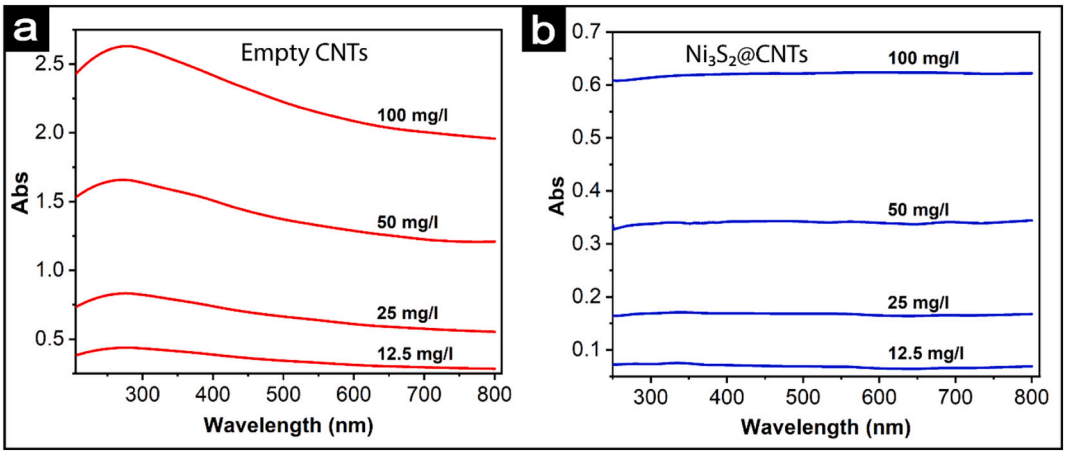

Fig. 7. UV–Vis spectra of (a) empty* CNTs and (b) Ni_3S_2@CNTs having different concentrations.
* Empty CNTs are independent of the filled CNTs and are only used as a reference to show the UV–Vis characteristics of typical empty MWCNTs.

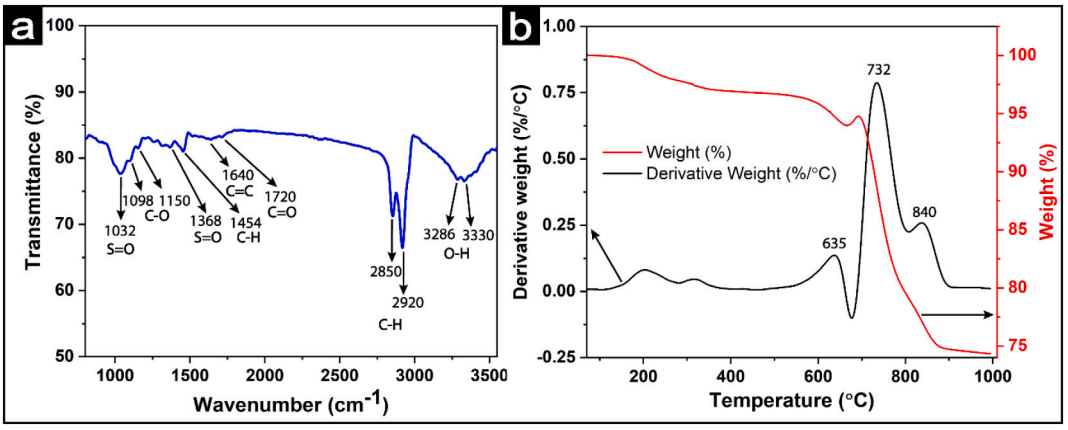

Fig. 8. (a) FTIR spectrum of Ni_3S_2@CNTs, (b) TGA analysis of Ni_3S_2@CNTs.

sp^3 C-H bending, [53] and the peak at 1640 cm^{-1} is due to C═C stretching [54]. Likewise, the IR peak at 1720 cm^{-1} can be assigned to the C═O stretching of carboxylic acid [55] whereas the peaks in the region of 3200–3570 cm^{-1} are due to the OH stretching of H-bonded water. It is important to note that Ni_3S_2@CNTs exhibit sharp and strong peaks at 2850 and 2920 cm^{-1} which are their characteristic peaks in the FTIR spectrum. These two peaks are due to the C-H stretching in CH, CH_2, and CH_3 groups [51,55] which are very weak in CNTs synthesized by other methods [56,57]. These peaks are, however, stronger in Ni_3S_2@CNTs due to the continuous flow of H_2 gas during the synthesis process which can ultimately functionalize the as-synthesized Ni_3S_2@CNTs by numerous alkyl groups. Fig. 8b represents the weight % (red curve) and derivative weight % (black curve) as a function of temperature. The peak observed at 635 °C is due to the oxidation of carbon walls which account for the very low weight (below 10 %) in the Ni_3S_2@CNTs. A strong peak located at 732 °C is due to the oxidation of Ni_3S_2. As Ni_3S_2 oxidizes to form NiO *via* metal oxosulfide intermediates (Ni_3SO + SO) [58] it causes an initial increase in weight as seen clearly in the red curve. Another major peak observed at 840 °C can be due to the oxidation of Ni present in the roots of the Ni_3S_2@CNTs. It is interesting to observe that only about 25 % weight loss occurred while burning the Ni_3S_2@CNTs at 1000 °C in the air. The final remainder was a greenish powder identified as NiO by the EDX analysis (Fig. S8).

3.6. *Opening of Ni_3S_2@CNTs tips*

Some applications of filled CNTs may require their tips to be opened such that the filling material is exposed, and its chemical activity is further enhanced. We successfully demonstrate two quick and reliable methods of opening the tips of Ni_3S_2@CNTs by using the acid treatment and plasma etching. Ni_3S_2@CNTs, as synthesized on the respective substrate, can be treated with 0.1 M HNO_3 for 5 min at room temperature which can cause the opening of the tips of most of the Ni_3S_2@CNTs as shown in Fig. 9a. The acid treatment can also induce some damage on the CNT walls as observed in Fig. 9b. Fig. 9c shows the opening of the Ni_3S_2@CNTs tips when the sample was treated with an oxygen plasma operating at a power of 200 W for 30 min. A small vacancy at the tip of most of the nanotubes in Fig. 9c demonstrates that the effect of the plasma begins from the sharper tips causing the removal of the tip particle and subsequent annihilation of several micrometers of the filler

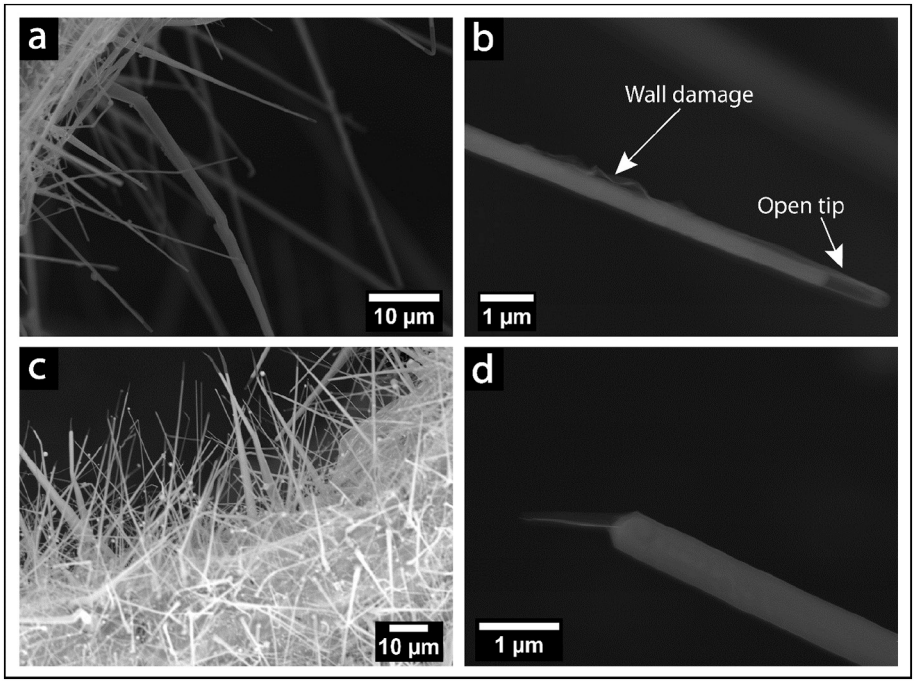

Fig. 9. SEM images of (a-b) acid opened Ni_3S_2@CNTs and (c-d) plasma opened Ni_3S_2@CNTs.

Ni_3S_2 near the tip region. Fig. 9d shows a plasma opened Ni_3S_2@CNT with a whisker like structure emanating at the tip which is possibly the exfoliated or stripped carbon shell remnant after plasma etching.

3.7. Electrical properties of Ni_3S_2@CNTs

The electrical properties of individual Ni_3S_2@CNTs were measured using both four-point probe and two probe methods. Firstly, Au electrodes (both four and two electrodes) were deposited on a SiO_2/Si wafer using photolithography as shown in Fig. 10a and b (AFM image in the inset). A very dilute suspension of Ni_3S_2@CNT-IPA was then made and 5 μl of it was dropped and spin-coated on the pre-patterned wafer containing the electrodes. The electrode system was immediately investigated in an optical microscope at an operating magnification of 100× to confirm if any single Ni_3S_2@CNT has passed across the electrodes. The process was repeated several times until a single Ni_3S_2@CNT was observed to pass through the Au electrodes. The wafer containing Au electrodes was cleaned in an ultrasonication bath after each trial to remove any cluster of Ni_3S_2@CNTs in the intermediate steps. Once a nanotube was found to make contacts with the electrodes, it was focused under a scanning electron microscope at higher magnifications (X5000 and above) and continuously welded using SEM electron beam by scanning the nanotube-electrode contact regions 5–10 times. This process can make a better contact between the Ni_3S_2@CNT and the Au electrodes before their I-V measurements.

Fig. 10a shows the SEM image of a Ni_3S_2@CNT in contact with four Au electrodes. Two samples A and B were used to determine the contact resistance between the Ni_3S_2@CNT and the Au electrodes by measuring the resistance of the same segment 2–3 using both four-probe and two probe measurements. It was found that the segment 2–3 of sample A measured resistance of 5.499 KΩ under four-probe measurements and resistance of 5.538 KΩ under two probe measurements. Similarly, another sample B measured the resistance values as 6.667 KΩ and 6.709 KΩ under four-probe and two probe measurements, respectively. Both these measurements revealed a very low contact resistance (about 40 Ohms) as compared to the intrinsic resistance of the segment of Ni_3S_2@CNT under investigation (5–7 KΩ). Thus, the two probe measurements were performed to estimate the resistivity of Ni_3S_2@CNT using ten different samples given the simplicity and accuracy of the two probe method in this case. The I-V characteristics of ten different Ni_3S_2@CNTs are shown in Fig. 10b whereas the I-V characteristics of samples A and B using four-probe and two probe measurements are shown in Fig. 10c and d, respectively. All these measurements show a linear I-V relationship in individual Ni_3S_2@CNTs. The measured electrical parameters and resistivities of each Ni_3S_2@CNTs are listed in Table 1 as shown below.

Fig. 11 shows the size-dependent electrical breakdown of individual Ni_3S_2@CNTs at higher currents. It was observed that Ni_3S_2@CNTs with smaller diameters (less than 150 nm) can undergo an electrical breakdown when an excessive current passes through them. As an example, Fig. 11a shows a thin CNT with a diameter of about 150 nm which eventually broke down as the current exceeded 0.8 mA. However, in the

Table 1
Estimation of the resistivity of individual Ni_3S_2@CNTs.

Ni_3S_2@CNT No.	Contact length (μm)	Diameter[a] (nm)	Resistance (KΩ)	Resistivity (Ωm)
1	4.1	255.4	7.2	8.9×10^{-5}
2	4.4	262.7	7.5	9.2×10^{-5}
3	5.1	131.4	9.2	2.4×10^{-5}
4	4.7	225.8	6.5	5.5×10^{-5}
5	4.2	274.6	5.6	7.8×10^{-5}
6	4.4	124.3	10.6	2.9×10^{-5}
7	6.0	204.8	9.8	1.7×10^{-5}
8	4.1	170.2	11.1	6.1×10^{-5}
9	4.8	256.5	6.7	7.2×10^{-5}
10	4.3	312.4	6.0	10^{-4}

Note: The resistivities were estimated assuming the Ni_3S_2@CNTs as three-dimensional solid cylindrical conductors.
[a] Within ±10 %.

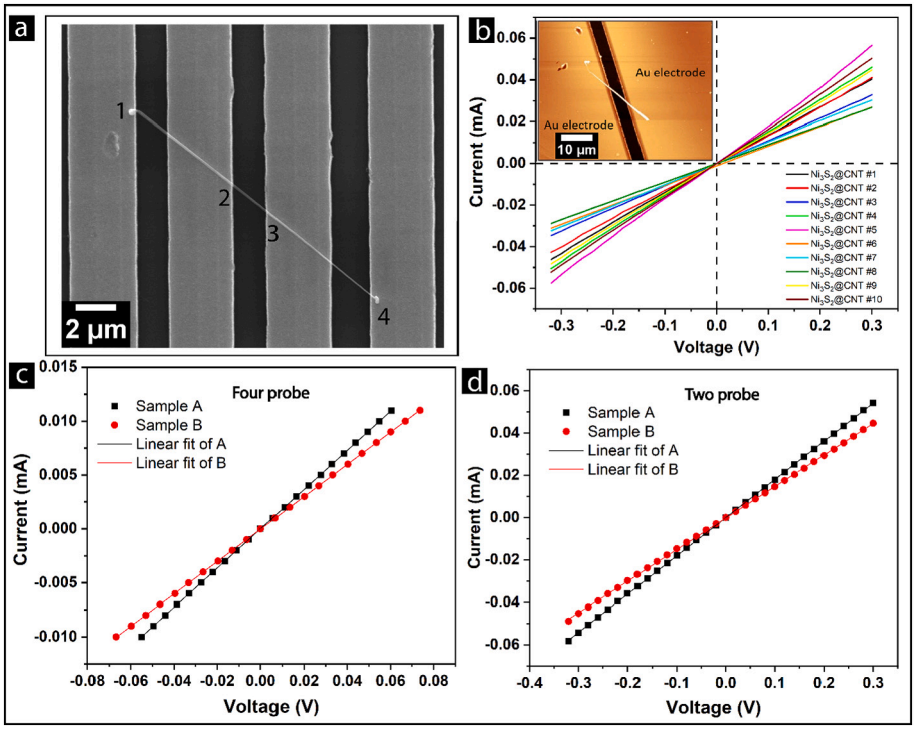

Fig. 10. (a) SEM image of a Ni_3S_2@CNT in contact with four Au electrodes, (b) I-V characteristics of ten different Ni_3S_2@CNTs measured using two probe method; inset shows an AFM image of an individual Ni_3S_2@CNT in contact with two Au electrodes, (c) I-V characteristics of the segment 2–3 (Fig. 10a) of two samples (A and B) measured using four-point probe method, and (d)) I-V characteristics of the segment 2–3 of the same samples (A and B) measured using two probe method.

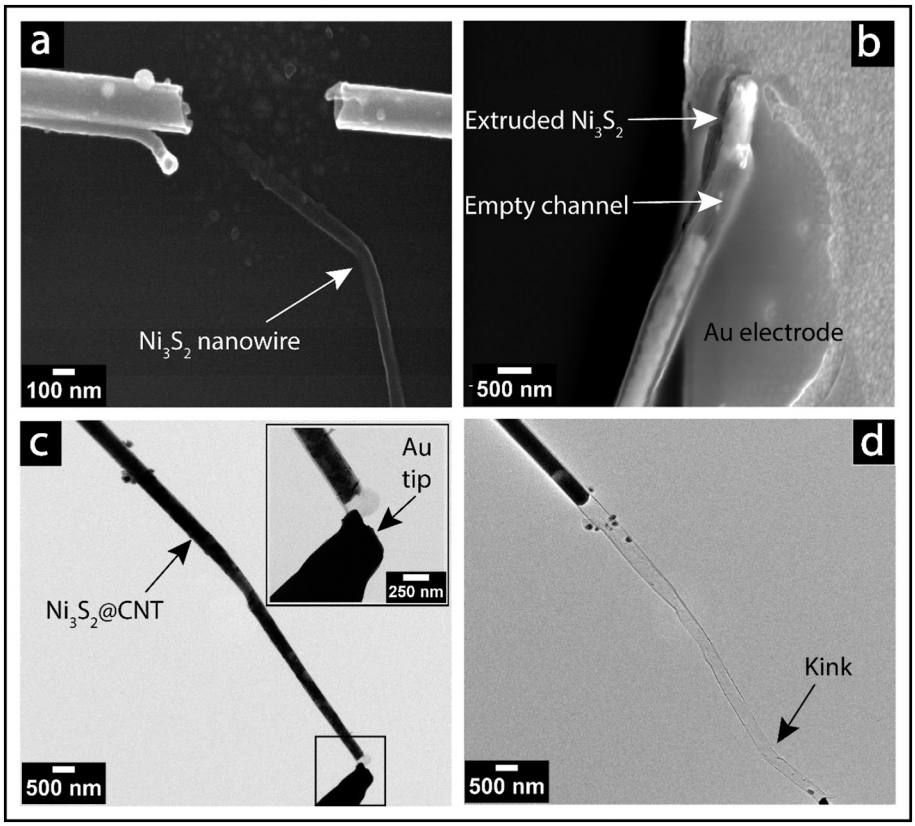

Fig. 11. SEM images showing (a) electrical breakdown of a thin Ni_3S_2@CNT and (b) electrical extrusion of Ni_3S_2 from the open end of Ni_3S_2@CNT when currents passing through the Ni_3S_2@CNTs in air. (c) *In situ* TEM image before passing the current, inset shows the connection between the gold tip and CNT walls of a broken segment of Ni_3S_2@CNT, and (d) *in situ* TEM image showing the current induced discharge of the Ni_3S_2 filler of the same Ni_3S_2@CNT. (For interpretation of the references to colour in this figure legend, the reader is referred to the web version of this article.)

case of empty MWCNTs, an electrical breakdown can occur at relatively smaller currents [59]. The reason Ni_3S_2@CNTs can pass a very high current is that a high proportion of current can pass through Ni_3S_2 core which has a low resistivity of 1.2×10^{-6} Ωm [32] thus preventing the rapid oxidation of CNT walls induced by the flow of current. If the diameter of Ni_3S_2@CNT is smaller than 150 nm, there are relatively fewer CNT walls that will suffer defects and damages as the magnitude of the current increases and can subsequently break down in fewer steps before the melting of Ni_3S_2 core caused by Joule heating. After the breakdown of Ni_3S_2@CNT, the Ni_3S_2 nanowire is ejected out of the breakdown region which can be seen in Fig. 11a. On the other hand, if the diameter of Ni_3S_2@CNT is greater, it doesn't break down even if a high amount of current (1 mA or above) passes through it. However, Ni_3S_2 nanowire can melt and extrude out from the open end of Ni_3S_2@CNT in the direction of the current flow. In this case, the melting temperature of Ni_3S_2 is reached before the breakdown of CNT walls. Fig. 11b illustrates an example of the electrical melting and extrusion of the Ni_3S_2 nanowire from a Ni_3S_2@CNT having a diameter of about 500 nm which was observed as the current exceeded 1 mA. The melting and discharge of the Ni_3S_2 filler at a higher current was also observed during *in situ* TEM experiment which can be seen in the supporting video file. Fig. 11c shows the TEM image of a Ni_3S_2@CNT having a diameter of about 280 nm (near the Au tip) which is continuously filled with Ni_3S_2 nanowire before passing any current. The inset shows the connection between the Au tip and the tip of a broken segment of Ni_3S_2@CNT. On applying a forward bias and increasing it slowly from 0 to higher volts, the Ni_3S_2 filler was melted and pushed in the direction of the current flow as a result of electromigration [64] which can be seen in the supporting video file 1 and Fig. 11d. Consequently, the empty section of the nanotube experienced mechanical stress causing a kink formation.

4. Conclusions

We have developed an *in situ* method to synthesize high-quality Ni_3S_2@CNTs on Si, nickel foam (NiF), and flexible carbon cloth (CC) substrates and characterized the samples using SEM, TEM, EDX, XRD, Raman, UV–Vis spectroscopy, FTIR, and TGA. The described method is simple, reliable, efficient, and scalable to grow a significant mass of Ni_3S_2@CNTs on NiF and CC substrates. TEM measurements show that CNTs are completely and continuously filled with single-crystalline Ni_3S_2 nanowires several micrometers in length. A very low I_D/I_G ratio of 0.26 observed in the Raman spectrum of Ni_3S_2@CNTs reveals that the CNT shells are highly crystalline and of excellent quality. Also, Ni_3S_2@CNTs show unusual absorption properties in the UV–Vis region because of the presence of Ni_3S_2 in the CNT cores. The intrinsic electrical properties of individual Ni_3S_2@CNTs were studied using both two probe and four-point probe methods and a mean resistivity of 6.1×10^{-5} Ωm was estimated. Also, a diameter selective electrical breakdown or nanowire propulsion was observed in Ni_3S_2@CNTs at higher currents. The solid core-shell structure with highly ordered carbon shells, better electronic conductivity, mechanical strength, and direct growth of Ni_3S_2@CNTs on conductive NiF and CC substrates make them promising candidates for various applications such as in energy storage devices (lithium-ion batteries and supercapacitors), electrocatalysis of water, nanoelectronics, *etc.*

Supplementary data to this article can be found online at https://doi.org/10.1016/j.diamond.2022.109156.

CRediT authorship contribution statement

Yuba Raj Poudel: Conceptualization, Methodology, Validation, Formal analysis, Investigation, Data curation, Visualization, Writing – original draft, Writing – review & editing. **Xu Zhao:** Methodology, Validation, Formal analysis, Investigation, Data curation, Writing – review & editing. **Katherine L. Jungjohann:** Formal analysis, Investigation, Validation, Writing – review & editing. **Arun Thapa:** Formal analysis, Investigation, Writing – review & editing. **Rui Guo:** Formal analysis, Investigation, Writing – review & editing. **Wenzhi Li:**

Conceptualization, Methodology, Validation, Formal analysis, Investigation, Resources, Data curation, Visualization, Writing – review & editing, Supervision, Project administration, Funding acquisition.

Declaration of competing interest

The authors declare the following financial interests/personal relationships which may be considered as potential competing interests:

Wenzhi Li and Yuba Raj Poudel have patent "FILLED CARBON NANOTUBES AND METHODS OF SYNTHESIZING THE SAME" (US patent 11,296,319 B1). Wenzhi Li and Yuba Raj Poudel have pending patent application "METAL SULFIDE FILLED CARBON NANOTUBES AND SYNTHESIS METHODS THEREOF" (https://patents.google.com/patent/US20210324537A1/en).

Acknowledgments

This work is supported by the National Science Foundation under grants 1506640 and 2134375. This work was performed, in part, at the Center for Integrated Nanotechnologies, an Office of Science User Facility operated for the U.S. Department of Energy (DOE) Office of Science. Sandia National Laboratories is a multi-mission laboratory managed and operated by National Technology and Engineering Solutions of Sandia, LLC., a wholly owned subsidiary of Honeywell International, Inc., for the U.S. DOE's National Nuclear Security Administration under contract DE-NA-0003525. This paper describes objective technical results and analysis. Any subjective views or opinions that might be expressed in the paper do not necessarily represent the views of the U.S. Department of Energy or the United States Government. We thank J. Su and Y. Gao (Huazhong University of Science and Technology, Wuhan, Hubei, P. R. China) for their help with the TEM experiment. We also thank C. Wang and A. Rabiei for their help with FTIR measurement, J. He and J. Guo for their help with the Raman measurement, and R. Raptis (Florida International University) for providing access to his laboratory for UV–Vis measurements. The authors would also like to acknowledge the support from the Advanced Materials Engineering Research Institutes (AMERI) at Florida International University.

References

[1] Y.R. Poudel, W. Li, Synthesis, properties, and applications of carbon nanotubes filled with foreign materials: a review, Mater. Today Phys. 7 (2018) 7–34, https://doi.org/10.1016/j.mtphys.2018.10.002.

[2] T.W. Odom, J.L. Huang, P. Kim, C.M. Lieber, Structure and electronic properties of carbon nanotubes, J. Phys. Chem. B 104 (13) (2000) 2794–2809, https://doi.org/10.1021/jp993592k.

[3] R. Saito, M. Fujita, G. Dresselhaus, M.S. Dresselhaus, Electronic structure of chiral graphene tubules, Appl. Phys. Lett. 60 (18) (1992) 2204–2206, https://doi.org/10.1063/1.107080.

[4] J.C. Charlier, X. Gonze, J.P. Michenaud, First-principles study of the electronic properties of graphite, Phys. Rev. B 43 (6) (1991) 4579–4589, https://doi.org/10.1103/PhysRevB.43.4579.

[5] A.H. Castro Neto, F. Guinea, N.M.R. Peres, K.S. Novoselov, A.K. Geim, The electronic properties of graphene, Rev. Mod. Phys. 81 (2009) 109, https://doi.org/10.1103/RevModPhys.81.109.

[6] M.M.J. Treacy, T.W. Ebbesen, J.M. Gibson, Exceptionally high Young's modulus observed for individual carbon nanotubes, Nature 381 (6584) (1996) 678–680, https://doi.org/10.1038/381678a0.

[7] P. Kim, L. Shi, A. Majumdar, P.L. McEuen, Thermal transport measurements of individual multiwalled nanotubes, Phys. Rev. Lett. 87 (21) (2001), 215502, https://doi.org/10.1103/PhysRevLett.87.215502.

[8] C.E. Cava, R. Possagno, M.C. Schnitzler, P.C. Roman, M.M. Oliveira, C. M. Lepiensky, et al., Iron- and iron oxide-filled multi-walled carbon nanotubes: electrical properties and memory devices, Chem. Phys. Lett. 444 (4–6) (2007) 304–308, https://doi.org/10.1016/j.cplett.2007.07.029.

[9] D. Golberg, P.M.F.J. Costa, M. Mitome, S. Hampel, D. Haase, C. Mueller, et al., Copper-filled carbon nanotubes: rheostatlike behavior and femtogram copper mass transport, Adv. Mater. 19 (15) (2007) 1937–1942, https://doi.org/10.1002/adma.200700126.

[10] R. Kumari, A. Singh, B.S. Yadav, D.R. Mohapatra, A. Ghosh, P. Guha, et al., Filled-carbon nanotubes: 1 D nanomagnets possessing uniaxial magnetization axis and reversal magnetization switching, Carbon 119 (2017) 464–475, https://doi.org/10.1016/j.carbon.2017.04.053.

[11] L. Camilli, M. Scarselli, S. Del Gobbo, P. Castrucci, F.R. Lamastra, F. Nanni, et al., High coercivity of iron-filled carbon nanotubes synthesized on austenitic stainless steel, Carbon 50 (2) (2012) 718–721, https://doi.org/10.1016/j.carbon.2011.09.034.

[12] Q. Su, J. Li, G. Zhong, G. Du, B. Xu, In situ synthesis of iron/nickel sulfide nanostructures-filled carbon nanotubes and their electromagnetic and microwave-absorbing properties, J. Phys. Chem. C 115 (5) (2011) 1838–1842, https://doi.org/10.1021/jp1113015.

[13] P. Xu, X.J. Han, X.R. Liu, B. Zhang, C. Wang, X.H. Wang, A study of the magnetic and electromagnetic properties of γ-Fe2O3–multiwalled carbon nanotubes (MWCNT) and Fe/Fe3C–MWCNT composites, Mater. Chem. Phys. 114 (2–3) (2009) 556–560, https://doi.org/10.1016/j.matchemphys.2008.10.010.

[14] R. Atchudan, T.N. Jebakumar Immanuel Edison, S. Perumal, D. RanjithKumar, Y. R. Lee, Direct growth of iron oxide nanoparticles filled multi-walled carbon nanotube via chemical vapour deposition method as high-performance supercapacitors, Int. J. Hydrog. Energy 44 (4) (2019) 2349–2360, https://doi.org/10.1016/j.ijhydene.2018.08.183.

[15] W.-J. Yu, C. Liu, P.-X. Hou, L. Zhang, X.-Y. Shan, F. Li, et al., Lithiation of silicon nanoparticles confined in carbon nanotubes, ACS Nano 9 (5) (2015) 5063–5071, https://doi.org/10.1021/acsnano.5b00157.

[16] S. Li, Y. Liu, P. Guo, C. Wang, Self-climbed amorphous carbon nanotubes filled with transition metal oxide nanoparticles for large rate and long lifespan anode materials in lithium ion batteries, ACS Appl. Mater. Interfaces 9 (32) (2017) 26818–26825, https://doi.org/10.1021/acsami.7b06394.

[17] P.V. Fedotov, A.A. Tonkikh, E.A. Obraztsova, A.G. Nasibulin, E.I. Kauppinen, A. L. Chuvilin, et al., Optical properties of single-walled carbon nanotubes filled with CuCl by gas-phase technique, Phys Status Solidi B 251 (12) (2014) 2466–2470, https://doi.org/10.1002/pssb.201451240.

[18] C. Soldano, F. Rossella, V. Bellani, S. Giudicatti, S. Kar, Cobalt nanocluster-filled carbon nanotube arrays: engineered photonic bandgap and optical reflectivity, ACS Nano 4 (11) (2010) 6573–6578, https://doi.org/10.1021/nn101801y.

[19] M. Monthioux, E. Flahaut, J.P. Cleuziou, Hybrid carbon nanotubes: strategy, progress, and perspectives, J. Mater. Res. 21 (11) (2006) 2774–2793, https://doi.org/10.1557/jmr.2006.0366.

[20] R. Kozhuharova, M. Ritschel, D. Elefant, A. Graff, A. Leonhardt, I. Mönch, et al., Synthesis and characterization of aligned Fe-filled carbon nanotubes on silicon substrates, J. Mater. Sci. Mater. Electron. 14 (10) (2003) 789–791, https://doi.org/10.1023/a:1026105304763.

[21] W.J. Yu, C. Liu, L. Zhang, P.X. Hou, F. Li, B. Zhang, Synthesis and electrochemical lithium storage behavior of carbon nanotubes filled with iron sulfide nanoparticles, Adv. Sci. (Weinh.) 3 (10) (2016), 1600113, https://doi.org/10.1002/advs.201600113.

[22] G. Korneva, H. Ye, Y. Gogotsi, D. Halverson, G. Friedman, J.C. Bradley, et al., Carbon nanotubes loaded with magnetic particles, Nano Lett. 5 (5) (2005) 879–884, https://doi.org/10.1021/nl0502928.

[23] J. Mittal, M. Monthioux, V. Serin, Photolysis-driven, room temperature filling of single-wall carbon nanotubes, J. Nanosci. Nanotechnol. 19 (7) (2019) 4129–4135, https://doi.org/10.1166/jnn.2019.16316.

[24] K. Yanagi, Y. Miyata, H. Kataura, Highly stabilized β-carotene in carbon nanotubes, Adv. Mater. 18 (4) (2006) 437–441, https://doi.org/10.1002/adma.200501839.

[25] S. Hampel, D. Kunze, D. Haase, K. Krämer, M. Rauschenbach, M. Ritschel, et al., Carbon nanotubes filled with a chemotherapeutic agent: a nanocarrier mediates inhibition of tumor cell growth, Nanomedicine 3 (2) (2008) 175–182, https://doi.org/10.2217/17435889.3.2.175.

[26] A.A. Tonkikh, D.V. Rybkovskiy, A.S. Orekhov, A.I. Chernov, A.A. Khomich, C. P. Ewels, et al., Optical properties and charge transfer effects in single-walled carbon nanotubes filled with functionalized adamantane molecules, Carbon 109 (2016) 87–97, https://doi.org/10.1016/j.carbon.2016.07.053.

[27] O.O. Balayeva, A.A. Azizov, M.B. Muradov, A.M. Maharramov, G.M. Eyvazova, R. M. Alosmanov, et al., β-NiS and Ni3S4 nanostructures: fabrication and characterization, Mater. Res. Bull. 75 (2016) 155–161, https://doi.org/10.1016/j.materresbull.2015.11.037.

[28] S. Saeed, N. Rashid, Growth and characterization of semiconducting nickel sulfide nanocrystals from air-stable single-source metal organic precursors, Cogent Chem. 1 (1) (2015), 1030195, https://doi.org/10.1080/23312009.2015.1030195.

[29] J. Li, P.K. Shen, Z. Tian, One-step synthesis of Ni3S2 nanowires at low temperature as efficient electrocatalyst for hydrogen evolution reaction, Int. J. Hydrog. Energy 42 (10) (2017) 7136–7142, https://doi.org/10.1016/j.ijhydene.2016.03.068.

[30] X. Guan, X. Liu, B. Xu, X. Liu, Z. Kong, M. Song, et al., Carbon wrapped Ni_3S_2 nanocrystals anchored on graphene sheets as anode materials for lithium-ion battery and the study on their capacity evolution, Nanomaterials (Basel) 8 (10) (2018) 760, https://doi.org/10.3390/nano8100760.

[31] N.K. Chaudhari, H. Jin, B. Kim, K. Lee, Nanostructured materials on 3D nickel foam as electrocatalysts for water splitting, Nanoscale 9 (34) (2017) 12231–12247, https://doi.org/10.1039/C7NR04187J.

[32] X. Song, X. Li, Z. Bai, B. Yan, D. Li, X. Sun, Morphology-dependent performance of nanostructured Ni3S2/Ni anode electrodes for high performance sodium ion batteries, Nano Energy 26 (2016) 533–540, https://doi.org/10.1016/j.nanoen.2016.06.019.

[33] W. Li, S.S. Xie, L.X. Qian, B.H. Chang, B.S. Zou, W.Y. Zhou, et al., Large-scale synthesis of aligned carbon nanotubes, Science 274 (5293) (1996) 1701, https://doi.org/10.1126/science.274.5293.1701.

[34] Z.W. Pan, S.S. Xie, B.H. Chang, C.Y. Wang, L. Lu, W. Liu, et al., Very long carbon nanotubes, Nature 394 (6694) (1998) 631–632, https://doi.org/10.1038/29206.

[35] J. Guo, J. Pan, S. Chang, X. Wang, N. Kong, W. Yang, et al., Monitoring the dynamic process of formation of plasmonic molecular junctions during single nanoparticle collisions, Small 14 (15) (2018) 1704164, https://doi.org/10.1002/smll.201704164.
[36] L. Wang, X. Li, Q. Li, X. Yu, Y. Zhao, J. Zhang, et al., Oriented polarization tuning broadband absorption from flexible hierarchical ZnO arrays vertically supported on carbon cloth, Small 15 (18) (2019), 1900900, https://doi.org/10.1002/smll.201900900.
[37] M.-S. Balogun, C. Li, Y. Zeng, M. Yu, Q. Wu, M. Wu, et al., Titanium dioxide@titanium nitride nanowires on carbon cloth with remarkable rate capability for flexible lithium-ion batteries, J. Power Sources 272 (2014) 946–953, https://doi.org/10.1016/j.jpowsour.2014.09.034.
[38] F.T. Chuang, P.Y. Chen, T.C. Cheng, C.H. Chien, B.J. Li, Improved field emission properties of thiolated multi-wall carbon nanotubes on a flexible carbon cloth substrate, Nanotechnology 18 (39) (2007), 395702, https://doi.org/10.1088/0957-4484/18/39/395702.
[39] S. Suzuki, S. Mori, The role of sulfur in promoted growth of carbon nanotubes in chemical vapor deposition proposed through the characterizations on catalytic nanoparticles, Appl. Surf. Sci. 471 (2019) 587–594, https://doi.org/10.1016/j.apsusc.2018.12.046.
[40] R.A. DiLeo, B.J. Landi, R.P. Raffaelle, Purity assessment of multiwalled carbon nanotubes by Raman spectroscopy, J. Appl. Phys. 101 (6) (2007), 064307, https://doi.org/10.1063/1.2712152.
[41] M. Dorina, A.C. Chipara, M. Chipara, Chipara, Raman spectroscopy of carbonaceous materials: a concise review, Spectroscopy 26 (2011) 42–47.
[42] S. Costa, E. Borowiak-Palen, M. Kruszyńska, A. Bachmatiuk, R.J. Kaleńzuk, Characterization of carbon nanotubes by Raman spectroscopy, Mater. Sci. 26 (2) (2008) 433–441.
[43] N. Feng, D. Hu, P. Wang, X. Sun, X. Li, Growth of nanostructured nickel sulfide films on ni foam as high-performance cathodes for lithium ion batteries, Phys. Chem. Chem. Phys. 15 (2013), https://doi.org/10.1039/c3cp50615k.
[44] Z. Cheng, H. Abernathy, M. Liu, Raman spectroscopy of nickel sulfide Ni3S2, J. Phys. Chem. C 111 (49) (2007) 17997–18000, https://doi.org/10.1021/jp0770209.
[45] J. Njuguna, O.A. Vanli, R. Liang, A review of spectral methods for dispersion characterization of carbon nanotubes in aqueous suspensions, J. Spectrosc. 2015 (2015) 11, https://doi.org/10.1155/2015/463156.
[46] T.T. Nguyen, S.U. Nguyen, D.T. Phuong, D.C. Nguyen, A.T. Mai, Dispersion of denatured carbon nanotubes by using a dimethylformamide solution, Adv. Nat. Sci. Nanosci. Nanotechnol. 2 (3) (2011), 035015, https://doi.org/10.1088/2043-6262/2/3/035015.
[47] P. Huang, C. Zhang, C. Xu, B. Le, Z. Li, Preparation and characterization of near-infrared region absorption enhancer carbon nanotubes hybridmaterials, Nano Biomed. Eng. 2 (2010), https://doi.org/10.5101/nbe.v2i4.p225-230.
[48] G.A. Rance, D.H. Marsh, R.J. Nicholas, A.N. Khlobystov, UV–vis absorption spectroscopy of carbon nanotubes: relationship between the π-electron plasmon and nanotube diameter, Chem. Phys. Lett. 493 (1) (2010) 19–23, https://doi.org/10.1016/j.cplett.2010.05.012.
[49] W. Cheung, M. Patel, Y. Ma, Y. Chen, Q. Xie, J.V. Lockard, et al., π-plasmon absorption of carbon nanotubes for the selective and sensitive detection of Fe3+ ions, Chem. Sci. 7 (8) (2016) 5192–5199, https://doi.org/10.1039/C6SC00006A.
[50] J. Yu, Y. Du, Q. Li, L. Zhen, V.P. Dravid, J. Wu, et al., In-situ growth of graphene decorated Ni3S2 pyramids on ni foam for high-performance overall water splitting, Appl. Surf. Sci. 465 (2019) 772–779, https://doi.org/10.1016/j.apsusc.2018.09.177.
[51] D. Jones, A.G. Scarlett, C.E. West, R.A. Frank, R. Gieleciak, D. Hager, et al., Elemental and spectroscopic characterization of fractions of an acidic extract of oil sands process water, Chemosphere 93 (9) (2013) 1655–1664, https://doi.org/10.1016/j.chemosphere.2013.03.011.
[52] T.L. Talarico, W.J. Dobrogosz, Chemical characterization of an antimicrobial substance produced by Lactobacillus reuteri, Antimicrob. Agents Chemother. 33 (5) (1989) 674–679, https://doi.org/10.1128/AAC.33.5.674.
[53] S. De, B.S. Satyanarayana, S. Sharma, K.M. Rao, Fourier-transform infrared absorption study of the nanocluster carbon thin films grown using cathodic arc process, AIP Conf. Proc. 1349 (1) (2011) 435–436, https://doi.org/10.1063/1.3605921.
[54] L.-S. Shi, L.-Y. Wang, Y.-N. Wang, The investigation of argon plasma surface modification to polyethylene: quantitative ATR-FTIR spectroscopic analysis, Eur. Polym. J. 42 (7) (2006) 1625–1633, https://doi.org/10.1016/j.eurpolymj.2006.01.007.
[55] B. Menezes, F. Ferreira, B. Silva, E. Simonetti, T. Bastos, L. Cividanes, et al., Effects of octadecylamine functionalization of carbon nanotubes on dispersion, polarity, and mechanical properties of CNT/HDPE nanocomposites, J. Mater. Sci. 53 (2018), https://doi.org/10.1007/s10853-018-2627-3.
[56] N.H. Metwally, G.R. Saad, E.A. Abd El-Wahab, Grafting of multiwalled carbon nanotubes with pyrazole derivatives: characterization, antimicrobial activity and molecular docking study, Int. J. Nanomedicine 14 (2019) 6645–6659, https://doi.org/10.2147/IJN.S182699.
[57] V. Bhaghavathi Parambath, R. Nagar, R. Vedarajan, N. Rajalakshmi, K. S. Dhathathreyan, R. Sundara, Synthesis of graphene-multiwalled carbon nanotubes hybrid nanostructure by strengthened electrostatic interaction and its lithium ion battery application, J. Mater. Chem. 22 (2012) 9949–9956, https://doi.org/10.1039/C2JM16294F.
[58] M. Marafi, A. Stanislaus, E. Furimsky, Environmental and safety aspects of spent hydroprocessing catalysts, in: M. Marafi, A. Stanislaus, E. Furimsky (Eds.), Handbook of Spent Hydroprocessing Catalysts (Second Edition), Elsevier, 2017, pp. 375–404.
[59] P.G. Collins, M. Hersam, M. Arnold, R. Martel, P. Avouris, Current saturation and electrical breakdown in multiwalled carbon nanotubes, Phys. Rev. Lett. 86 (14) (2001) 3128–3131, https://doi.org/10.1103/PhysRevLett.86.3128.
[60] P.M.F.J. Costa, U.K. Gautam, M. Wang, Y. Bando, D. Golberg, Effect of crystalline filling on the mechanical response of carbon nanotubes, Carbon 47 (2) (2009) 541–544, https://doi.org/10.1016/j.carbon.2008.11.031.